In situ TEM observations of ion irradiation damage in boron carbide

Guillaume Victor, Yves Pipon, Nathalie Moncoffre, Nicolas Bererd, Claude Esnouf, Thierry Douillard, Aurélie Gentils

Version of Record: https://www.sciencedirect.com/science/article/pii/S0955221918306769
Manuscript_6cae335a4c692148ca3e82c3e1cbc9ce

In situ TEM observations of ion irradiation damage in boron carbide

G. Victor [a], Y. Pipon [a,b,*], N. Moncoffre [a], N. Bérerd [a,b], C. Esnouf [c], T. Douillard [c], A. Gentils [d]

[a] Université de Lyon, UCBL, Institut de Physique Nucléaire de Lyon, Villeurbanne, France

[b] Université de Lyon, UCBL, IUT chimie Lyon-1, Villeurbanne, France

[c] Université de Lyon, INSA de Lyon, MATEIS UMR CNRS 5510, Villeurbanne, France

[d] CSNSM, Université Paris-Sud, CNRS/IN2P3, Université Paris-Saclay, Orsay, France

Abstract

This paper presents an *in situ* Transmission Electron Microscopy (TEM) study of the damage formation process in ion-irradiated boron carbide used as neutron absorber for fast nuclear reactors. We focused our experiment on the damage induced by 1 MeV gold ions irradiation performed on the JANNuS-Orsay *in situ* dual ion beam TEM facility. The effects of the crystallographic orientation and the temperature (RT, 500 °C and 800 °C) on the ion-irradiated boron carbide structure were studied. The different steps of damage formation leading to amorphization are described. At RT, material amorphization is observed at a damage dose threshold around 7.5 displacements per atom (dpa). It is also shown that no amorphization occurred when irradiation is performed at 500 °C or 800 °C up to the highest fluence studied (3×10^{15} ions.cm^{-2}, i.e. 7.6 dpa).

Keywords: *in situ* TEM, boron carbide, irradiation damage, amorphization

*** Corresponding author:** Yves PIPON

E-mail: y.pipon@ipnl.in2p3.fr

Postal address: Université de Lyon, UCBL, IPNL, Campus LyonTech La Doua, 4 rue Enrico Fermi, 69622 Villeurbanne cedex, France

1. Introduction

Because of its excellent physical properties, boron carbide (B_4C) is a ceramic widely studied. Its super-hardness [1], high Hugoniot elastic limit (HEL ~ 17 GPa) combined with a low density make boron carbide a material of interest for military applications, like shields or bullet proof vests for instance. Moreover, the high neutron absorption cross-section of ^{10}B makes the boron carbide of particular interest for nuclear reactors [2, 3]. Indeed, boron carbide is one of the principal material used as neutron absorber in Light Water Reactors (LWR) and the most promising material for neutron absorber in the future generation of Sodium Fast Reactors (SFR) [4]. Especially, boron carbide was chosen to be the neutron absorber material in the French prototype nuclear reactor ASTRID (Advanced Sodium Technological Reactor for Industrial Demonstration) [5, 6]. This reactor is supposed to launch the fourth generation of nuclear reactors in France by proving the feasibility of this technology in the years to come. This choice results mainly from a low cost and a good availability of the raw materials. Boron carbide is also known for its great resistance under irradiation during reactor operation, attributed in most studies to its complex crystallographic structure [7, 8]. In its idealized form, the boron carbide structure consists of one icosahedron (12 atoms) and one linear 3-atoms chain. Icosahedra are linked together through six atoms in “polar” sites and bonded to the chains through the other six atoms in “equatorial” sites. Icosahedra are found at the vertices of a rhombohedral unit cell (space group $R\bar{3}m$) while the chain connects the icosahedra along the [111] rhombohedral axis [9]. The structure can also be represented as a hexagonal lattice (non primitive cell) where the [0001] axis of the hexagonal lattice corresponds to the [111] of the rhombohedral one. Exact sites of occupancies are debated in the literature, but *ab initio* calculations found that the most probable configuration for B_4C is $(B_{11}C^p)CBC$ [10]. In this configuration, $(B_{11}C^p)$ stands for an icosahedron with a carbon atom on a “polar” (C^p) site, whereas CBC stands for the 3-atoms carbon-boron-carbon chain. However, B and C atoms can be interchangeable, constituting the large range homogeneity of the B-C system, currently named B_4C, but with phases existing from B_4C to $B_{10}C$ [11, 12]. Figure 1 presents the $(B_{11}C^p)CBC$ structure of boron carbide (hexagonal representation).

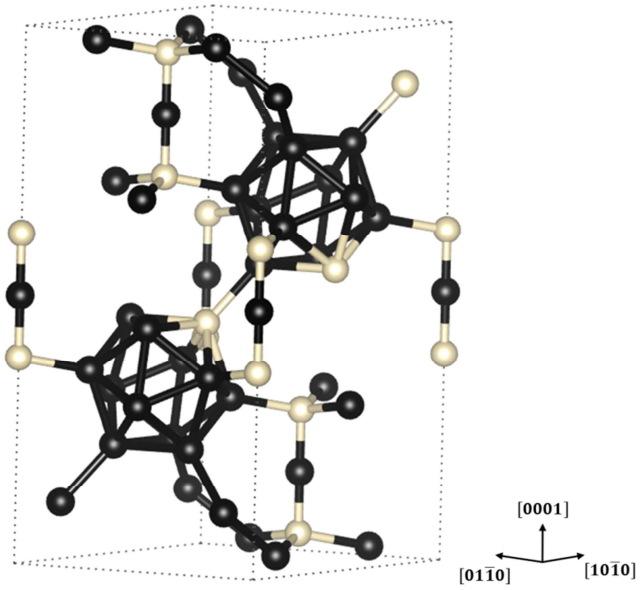

Figure 1 *(1 column)* **-** *Scheme of the ($B_{11}C^{p}$)CBC boron carbide structure (hexagonal representation). White spheres represent carbon atoms; black spheres represent boron atoms.*

Structural modifications and amorphization of boron carbide has been widely studied under different conditions. It is now well known that boron carbide undergoes an amorphization transition under high-velocity impacts reducing its strength, which is a major problem in the context of bullet proof vest. Therefore, most literature papers deal with the study of the amorphization process of boron carbide under stress [13-17]. For instance, Zhao *et al.* [18] have performed laser shock compression on boron carbide samples. They have highlighted that shear stresses lead to large magnitude atomic displacements, which are dissipated by competing mechanisms such as amorphization, cleavage and dislocation formation. Most studies [19-21] have pointed out that amorphization in boron carbide can be described as the inhomogeneous loss of crystalline order in small zones scattered within a volume influenced by a high-pressure event. However, the mechanisms at an atomic scale are unclear and some disagreements arise from the literature. Several studies have shown that icosahedra retain their structural integrity after amorphization and that the primary mechanism responsible for initiating amorphization is the bending of the linear chains (see for instance [22]). However, Xie *et al.* [23], who have performed laser-assisted atom probe tomography, have shown that the icosahedra in boron carbide are not as stable as previously anticipated and that the chain–icosahedron bonds are stronger than expected. This suggests that chain–icosahedra interactions can trigger shear amorphization.

In the context of nuclear power plants, post-irradiation examinations have shown some structural modifications of boron carbide but without amorphization [24, 25]. To separate the different parameters occuring during reactor operation, irradiation experiments can be performed with charged particles of different kinds. Ballistic damage, which is predominant in

B_4C due to neutron irradiation that creates elastic collisions, can be simulated by heavy ions at low energy. To a much lower extent, there can also be electronic damage mainly due to the fission products and the energetic recoiling atoms. This effect can be simulated by light ions, swift ions or electrons irradiations. Kushita *et al.* [26] have observed by *in situ* EELS (Electron Energy Loss Spectroscopy) and TEM, the amorphization of boron carbide irradiated with H_2^+ ions (16 keV) and/or He^+ ions (12 keV). They have shown that boron carbide became amorphous from a threshold fluence of 2.5×10^{17} $(H^+).cm^{-2}$ or 4×10^{16} $ions.cm^{-2}$ when performing irradiation with both ions simultaneously. Maruyama *et al.* [27] have studied the amorphization of boron carbide irradiated by He ions at two different energies: 15 MeV and 100 keV for fluences up to 2×10^{17} $ions.cm^{-2}$. The authors observed an amorphization for the 15 MeV He irradiation but never for the 100 keV He irradiation. Victor *et al.* [28] have made a preliminary study involving irradiation of boron carbide by iodine ions at 100 MeV. They have shown by positron annihilation spectroscopy (PAS) and by Raman spectroscopy that irradiation at room temperature (RT) creates damage in the structure but that the same irradiation at 800 °C anneals the structure to the point that there was no measurable damage. Very few experiments have been performed with heavy ions. Gosset *et al.* [29, 30] have examined, by TEM and Raman spectroscopy, boron carbide samples which were previously irradiated with 4 MeV Au^+ ions at room temperature (RT) and at different fluences. The samples were amorphized above a threshold fluence of 2×10^{15} $ions.cm^{-2}$. For irradiations with mainly ballistic collisions, the amorphization threshold should be therefore defined in function of the mean displacements per atom (dpa) value, which mainly depends (for a same target) on the nature of the incident ion, its energy and the irradiation fluence. Some irradiations on boron carbide samples have also been performed with electrons [31, 32]. Even if amorphization has been observed with 2 MeV electron irradiation (with a very high fluence of 1.3×10^{24} $e.cm^{-2}$ and at 106 K), the literature puts forward a good resistance of the material due to the really stable icosahedron “cage” structure able to self-anneal under electron irradiation [33].

In this study, we will focus specifically on the formation of damage induced by ballistic collisions. In order to investigate in more details the mechanisms of boron carbide amorphization created by ballistic damage, an *in situ* TEM irradiation experiment with 1 MeV Au^+ ions was carried out at the JANNuS-Orsay facility [34]. *In situ* TEM is a very powerful technique to observe the dynamic defect formation as it allows in real-time the analysis of radiation induced microstructural changes. In this paper, we will describe the steps of defect formation leading to the material amorphization process and discuss the possible effects due to crystallographic orientations and temperature.

2. Material and methods

This section provides information on the preparation of the boron carbide samples from the powder to the thin foils and on the irradiation conditions.

2.1 Boron carbide sample preparation

HD20 boron carbide powder bought from H.C. Starck was shaped and sintered using the non-conventional Spark Plasma Sintering (SPS) method [35, 36] at IRCER Limoges (France). The pellets were shaped in the form of cylinders (Ø = 10 mm and 5 mm thick). The sintering conditions are fully described in a previous paper [28]. The mean grain size of the boron carbide samples was measured at 660 ± 250 nm.

From the pellets, four thin foils were prepared by the Focused Ion Beam (FIB) technique at the *"Centre Lyonnais de Microscopie"* (CLYM) at INSA Lyon (France). Afterwards, they were positioned on four different molybdenum grids. Molybdenum was chosen for its good resistance at high temperature. The surfaces of the thin foils are around 10×3 µm^2 (Figure 2a), and their thicknesses differ from 80 to 210 nm, as detailed in the next paragraph. The thin foils will be named F_1, F_2, F_3 and F_4 depending on their thickness.

2.2 Thin foil characterization

The characteristics of each thin foil were controlled by TEM after fabrication in order to verify their quality and their crystallinity. The TEM images did not display any defects introduced by the FIB preparation. The principal observation is the presence of some twinned crystals in the thin foils (showed by red arrows in Figure 2a) due to the sintering process.

Transmission Kikuchi Diffraction (TKD) analyses were carried out on each thin foil. TKD, is an electron diffraction method used in Scanning Electron Microscope (SEM) that provides quantitative microstructural information about the crystallographic features (grain size, grain boundary, grain orientations, texture…) of most inorganic materials [37, 38]. In our study, the principal interest of TKD was to map the crystallographic orientation of each grain and to further consider the possibility of orienting a crystallographic axis parallel to the ion beam. Figure 2b shows the result of the TKD analysis on the thin foil F_2. Each color corresponds to a different orientation, as it is shown in the standard stereographic projection in hexagonal axis.

Each thin foil contains more than a hundred grains with different grain orientations. To study the role of the crystallographic orientation on the damage formation, we chose several adjacent grains in each thin foil where the *in situ* TEM observations have been focused. For instance, different zone axis (always parallel to the ion beam) have been identified from a stereographic projection work. Two of them are shown in Figure 3. The micrograph in Figure 3a is oriented along the $[5\,\bar{1}\,\bar{4}\,0]$ axis where the structural elements, chains and icosahedra, are superimposed. In Figure 3b, the boron carbide structure is oriented along the $[1\,\bar{2}\,1\,0]$ axis where the 3-atom chains are well exposed. As explained in the previous part, the boron

carbide resistance under irradiation is in general correlated with the resistance of the icosahedral structure. In our experiment, one objective was to determine if the chains were more likely to break under irradiation rather than the icosahedron and which one is responsible for the principal damage created in the material.

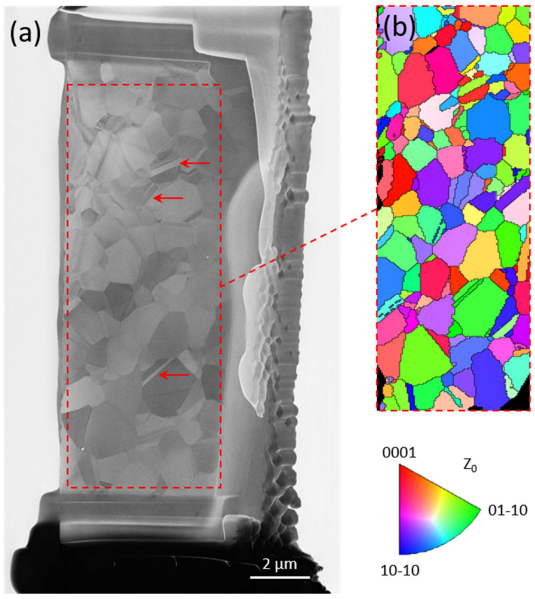

Figure 2 *(1 column)* **-** *SEM micrography of the F_2 thin foil (a) and the respective TKD map (b) displayed in inverse pole figure (IPF) coloring and acquired at the CLYM (INSA).*

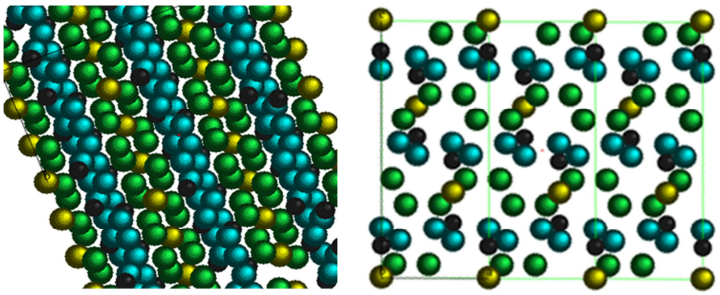

Figure 3 *(1 column)* **-** *Projected views for two orientations (a) and (b) of the boron carbide structure. In green: first 18h Wyckoff position – blue: second 18h Wyckoff position – yellow: 3a – black: 6c.*

The thickness of each thin foil is assessed with the commonly used log-ratio method using EELS [39] and the compute thickness routine implemented in Digital Micrograph software (Gatan, Pleasanton, United States), with a collection semi-angle of 11.8 mrad at 200 keV. The measured average thicknesses are respectively 80 nm, 150 nm, 180 nm and 210 nm from F_1 to F_4 and are named t_{F1} to t_{F4} in this paper, with a standard deviation of 5 nm.

2.3 Irradiation conditions

The *in situ* TEM ion irradiation experiment was done at the JANNuS-Orsay facility at SCALP / CSNSM, Orsay, France, part of the French EMIR accelerator network [40]. The JANNuS-Orsay facility holds a 200 kV FEI Tecnai G^2 20 TEM linked to two home-made accelerators, a 2 MV Van de Graaff/Tandem (ARAMIS) and a 190 kV implantor (IRMA), giving the possibility of a double ion beam irradiation of materials simultaneously with TEM observation and analysis. In our experiment, only a single ion beam coming from ARAMIS accelerator was used. During the experiment, a double tilt sample holder enables us to position the thin foil in front of the electron beam for the TEM observations, or in front of the ion beam coming from the accelerator during the irradiation, or in front of both (depending on the chosen grain size orientation, see details later). Moreover, based on a stereographic projection work from TKD data, some zone axis of crystals were aligned with the ion direction, especially for the thin foil called F2 (see table 1).

The irradiations were performed with 1 MeV Au^+ ions, in order to maximize the created ballistic damage (dpa) in the material. The mean flux of the ion beam was kept below 2.5×10^{11} ions.cm^{-2}.s^{-1} in order to prevent any excessive heating of the sample. The thin foils were tilted off the optical axis of the microscope, using the alpha and beta angles of the TEM specimen holder, so that the Au ion beam makes an angle of 52° with respect to the surface normal direction of the F_1, F_2 and F_3 thin foils, and an angle of 63° with respect to the surface normal direction of the F_4 thin foil. The SRIM 2013 software [41] was used in the full cascade mode in order to calculate the dpa profile and the gold concentration profile in boron carbide samples (bulk density of 2.5 g.cm^{-3}). The displacement energy thresholds used for the calculations are respectively of 28 eV and 25 eV for C and B. Figure 4 presents the results obtained with SRIM for an irradiation with 1 MeV Au^+ ions at a fluence of 10^{15} ions.cm^{-2} and an incident angle of 52°. Figure 4a presents the damage profile and the Au concentration profiles and Figure 4b presents the evolution of the electronic and nuclear stopping power of boron carbide irradiated with 1 MeV Au^+ ions as a function of depth.

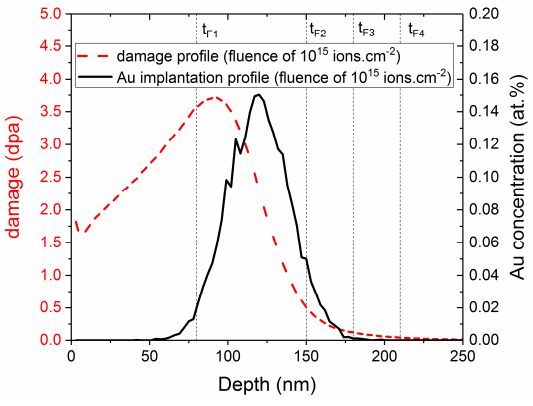

Figure 4a – *Damage and implantation profiles of 1 MeV Au^+ ions in B_4C calculated with SRIM software. t_{F1} to t_{F4} indicate the thickness value of each thin foil.*

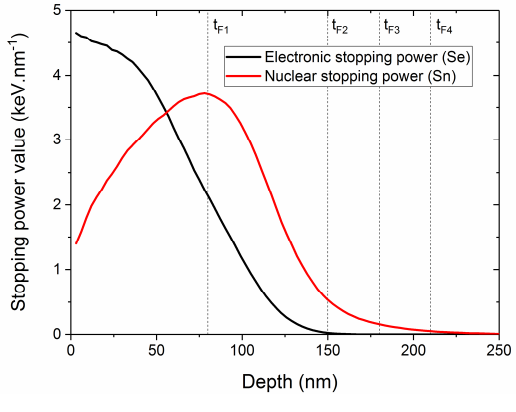

Figure 4b – *Electronic and nuclear stopping power of B_4C irradiated by 1 MeV Au^+ ions, as extracted from SRIM software. t_{F1} to t_{F4} indicate the thickness value of each thin foil.*

For an irradiation fluence of 10^{15} ions.cm^{-2}, the damage profile varies from 1.8 dpa at the surface to a maximum of 3.7 dpa at a depth of 95 nm from the surface. The implantation profile of Au^+ ions displays a quasi-Gaussian curve with a maximum concentration of 0.15 at. % at 120 nm (which is called R_p for projected Range). For F_2 thin foil (t_{F2}= 80 nm), all the Au^+ ions passed through the thin foil whereas for F_1 and F_3 thin foils (thicknesses of 150 nm and 180 nm, respectively), most Au^+ ions remained implanted in the thin foils. For the F_4 thin foil (t_{F4} = 210 nm), the gold concentration profile displays a quasi-Gaussian curve centered at 90 nm (not shown here) and all the Au^+ ions are implanted in the thin foil. We can see from figure 4b that the main drawback when using heavy ions, as gold ions, is that the electronic stopping power is never negligible. In our experiment, the electronic stopping power has a value of 4.7 keV.nm^{-1} at the surface. Its possible impact will be discussed later.

The irradiations were made at RT (F_1 and F_2 thin foils), 500 °C (F_3 thin foil) and 800 °C (F_4 thin foil). These temperatures were chosen to simulate the temperature of the boron carbide (500°C to 800°C approximately) in a SFR nuclear reactor [42]. The heating rate was of 20 °C per min until 500 °C and of 40 °C per min from 500 °C to 800 °C. No modification of the crystallographic structure was observed during the rise of temperature until 800 °C. During the ion irradiation experiment, a wide angle camera was used to record the thin foil's microstructure evolution. It was possible to stop the ion irradiation at any time to characterize in more details the observed structural modifications.

All the experimental conditions are summarized in Table 1. Each dpa value indicated in the table is an averaged value integrated on the dpa profiles from the surface up to the t_{F2} value for F_2 or up to t_{F1} for F_1, F_3 and F_4. It must be noted that the dpa values given for F_3 and F_4 are only indicative, as temperature is known to anneal defects.

Sample	**Thickness « t » (nm) ± 5 nm**	**Irradiation temperature (°C)**	**Fluences ($10^{14}Au^+.cm^{-2}$)**	**Average value of dpa at each fluence step**	**Orientation**
F_1	~ 150	RT	10 – 13	2.46 – 3.20	Random
F_2	~ 80		0.1 – 1.3 – 2.3 - 3.3 – 10 – 13 – 15 – 18 – 25 – 30 – 40	0.03 – 0.33 – 0.58 – 0.84 – 2.54 – 3.30 – 3.80 – 4.57 – 6.34 – 7.61 – 10.15	[5 $\bar{1}$ $\bar{4}$ 0] [1 $\bar{2}$ 1 0]
F_3	~ 180	500	1.3 – 10 – 30	0.32 – 2.46 – 7.38	Random
F_4	~ 210	800	1.3 – 10 – 30	0.32 – 2.48 – 7.43	Random

Table 1 - *Summary of the experimental conditions of the in situ TEM ion irradiations at JANNuS Orsay. The mean flux of the ion beam was 2.5×10^{11} ions.cm^{-2}.s^{-1}.*

The first RT ion-irradiation of the F_1 thin foil was recorded all along with the camera. A TEM micrograph was taken at a fluence of 1×10^{15} ions.cm^{-2} (~1.7 dpa at 100 nm), to characterize

in more details the modifications of the material. For the F_2 thin foil, we performed TEM images at more fluence steps, from 10^{13} ions.cm^{-2} (0.03 dpa) to 4×10^{15} ions.cm^{-2} (10.15 dpa) as indicated in Table 1.

The irradiations of F_3 (500 °C) and F_4 (800 °C) were observed at three fluences indicated in Table 1. The observed behavior at both temperatures being similar, they are described at the same time in the following part.

3. Results

3.1 Irradiation at RT

We start describing Figure 5 that presents the bright field images and the corresponding diffraction patterns of F_1 before irradiation (Figure 5a) and at two different irradiation fluences: 10^{15} ions.cm^{-2} (Figure 5b) and 1.3×10^{15} ions.cm^{-2} (Figure 5c). The important deformation of the thin foil during the ion irradiation (see Figure 7) makes difficult the indexation of the diffraction patterns. However the diffraction orientation g selected in (Figure 5b) and (Figure 5c) seems to be {-1101} type.

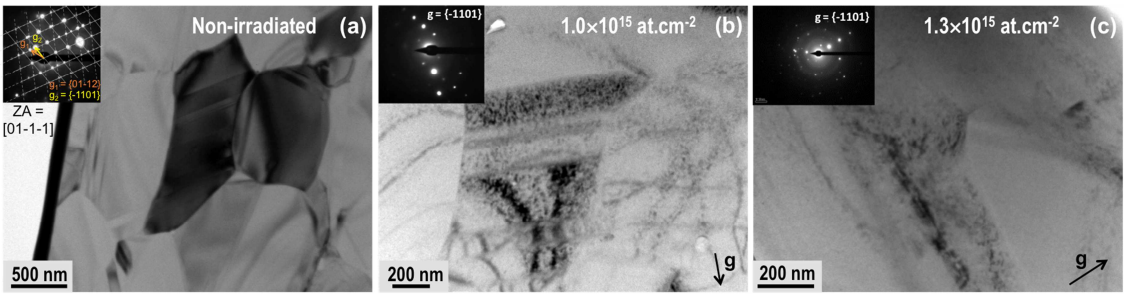

Figure 5 – *Bright field images showing the evolution of F_1 thin foil before 1 MeV Au ion irradiation at RT and at 2 fluences: (a) non irradiated, (b) 1×10^{15} ions.cm-2, (c) 1.3×10^{15} ions.cm^{-2}. The corresponding diffraction patterns are shown in top-left insets.*

In between the beginning of irradiation and the fluence of 10^{15} ions.cm^{-2} (around 2.5 dpa), the bright field (BF) images show an evolution of the crystalline contrast. The evolution of contrasts inside grains (bend contours) can be attributed to: i) a global tilt of the sample – ii) a local bending of lattice planes due to dilatation of superior or inferior part of the thin foil – iii) the superposition of i) and ii) effects. In our experiment, the crystal curvature causes a change of the aspect of the bend contours that appear narrower with parallel fringes around the principal contour. Moreover, when bend contours inside a grain disappeared, a slight tilt of the sample is enough to make the re-appearance of the bend contours. We can therefore conclude that even if a small global tilt exists, the major phenomenon is a local bending of the crystal attributed to an irradiation effect such as point defect production and accumulation. At the end of the irradiation of F_1 thin foil at a fluence of 1.3×10^{15} ions.cm^{-2} (3.2 dpa), the crystalline contrasts are almost invisible in Figure 5c and the SAED pattern

shows the emergence of diffuse diffraction rings superimposed to the crystal diffraction spots, revealing the beginning of the material's amorphization.

In order to identify those defects, a dark field (DF) image was taken on the F_1 thin foil with a g equal to {-1 1 0 1}. It highlights that those defects seem to correspond to dislocation loops ~~contrasts (red arrows)~~ of 20 nm approximately, as suggested by the observed coffee-bean like contrast (red arrows).

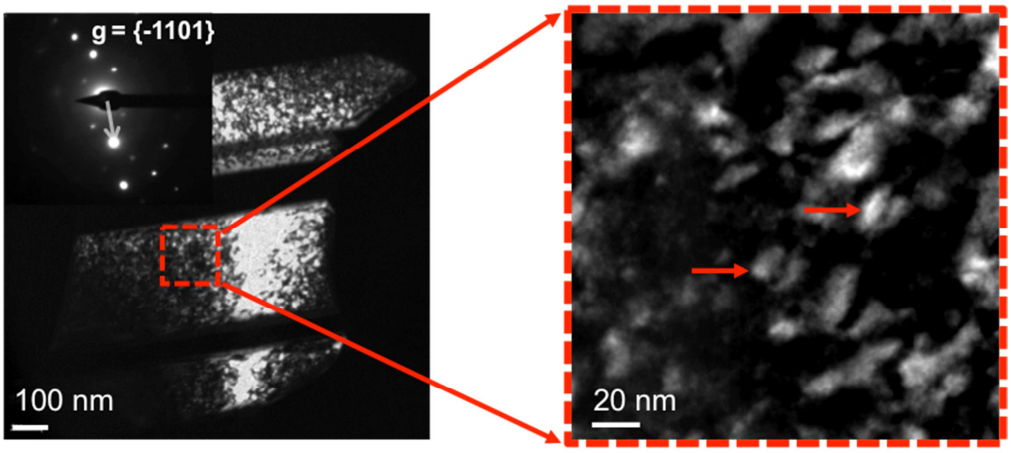

Figure 6 *(1 column)* **–** *Dark field image of F_1 thin foil after 1 MeV Au^+ ion irradiation at RT at a fluence of 1×10^{15} ions.cm^{-2}. The image on the right shows an enlargement of the left image. The red arrows point to coffee-bean like contrasts, attributed to dislocation loops* ~~*contrasts*~~*.*

After completing the irradiation, a detailed observation of the entire F_1 thin foil showed us differences between the *in situ* TEM observed area, undergoing the effect of ions and electrons, and the rest of the thin foil, undergoing only the effect of ions. The TEM image in Figure 7 shows the upper-half of the F_1 thin foil after ion irradiation. Two different areas (marked by red rectangles) and their corresponding SAED patterns (a and b), show the effect of the electron beam on the microstructural behavior of the thin foil. The material is completely amorphous except in the part observed with the electron beam *in situ* during the ion irradiation. This electron-induced artifact can be responsible for a self-healing of the material structure during ion irradiation, as it was observed in silicon for instance [43-44]. Another evidence of induced stresses is observed in Figure 7. In the circled zone (white circle), the thickness is smaller, due to local excess of FIB thinning. Therefore, stresses are more easily relaxed in this region, with as consequence a large deformation of the thin foil showed by a folding of the thin foil.

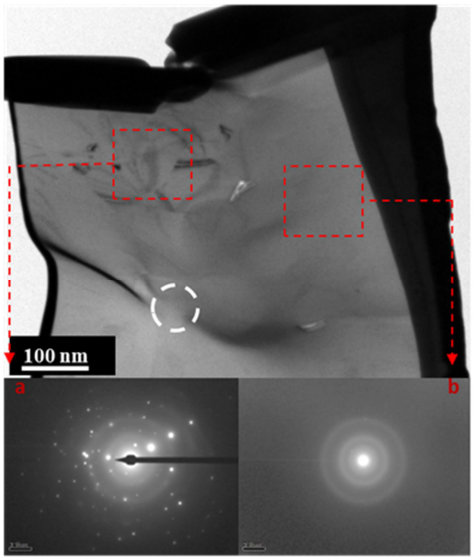

Figure 7 *(1 column)* – *SAED patterns taken in two different areas of thin foil F_1 after irradiation (1.3×10^{15} ions.cm^{-2}). (a) Area observed in situ with the electron beam during irradiation; (b) Area observed only after the end of the ion irradiation. The white circle shows the thinner part of the lamella responsible of a folding of the thin foil during ion irradiation.*

For the second RT irradiation (F_2 thin foil), *in situ* Au^+ ion irradiations were performed without exposing the thin foil to the electron beam, except during short image acquisition at different fluence steps. Figure 8 presents the bright field images and the corresponding diffraction patterns of F_2 before irradiation (Figure 8a) and at five chosen irradiation steps (Figure 8b to Figure 8f).

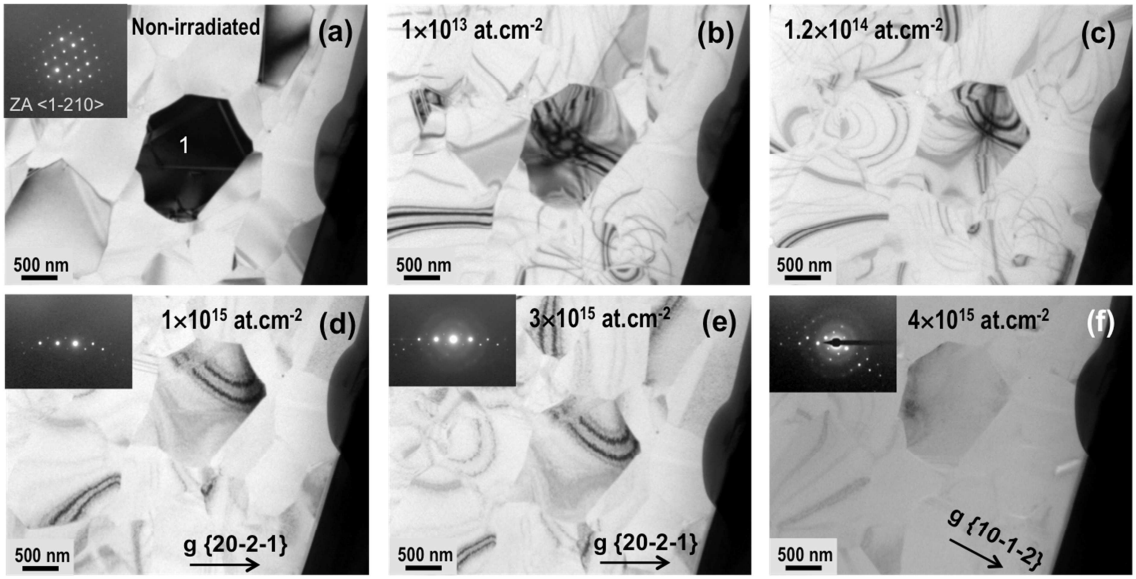

Figure 8 - *Bright field images showing the evolution of F_2 thin foil irradiated with 1 MeV Au^+ ions at RT at several fluences as indicated, from (a) non-irradiated to (f) 4×10^{15} at.cm^{-2}. The dark grain labelled 1 in (a) has the zone axis [1 $\bar{2}$ 1 0], up to the 1.2×10^{14} at.cm^{-2} fluence. After the fluence of 1×10^{15} at.cm^{-2}*

(d), the selected diffraction orientation is g = {20-2-1}. At 4x10^{15} at.cm^{-2}, the g orientation is different because of the bending of the thin foil.

In Figure 8b, the appearance and the displacement of the diffraction fringes (Bragg contours) inside the dark grain displayed in (8a), are due to an important material stress and a local curvature of the thin foils. This phenomenon, already observed on F_1, occurred as soon as the irradiation started.

The central grain (with the number “one” indicated in Figure 8a) is placed in exact Bragg position and the bend contour fills the whole grain area showing that the crystal is completely relaxed (bending or stress absences). Just after the irradiation started, bend contours appear inside the grain originated by several diffraction waves. Progressively, as the irradiation fluence increases, they shift until only one bend contour of one wave subsists for an irradiation fluence around 2×10^{14} ions.cm^{-2} (around 0.5 dpa). The appearance of these bend contours is unambiguously due to a local distortion (dilatation) of crystal originated by the irradiation. Then, no significant modifications are observed until an irradiation fluence of 3×10^{15} ions.cm^{-2} (around 7.6 dpa). At this fluence, the SAED pattern shows a light halo in addition to the crystal diffraction spots, announcing the beginning of the amorphization process. At the end of the irradiation (4×10^{15} ions.cm^{-2}, around 10 dpa), the bend contour has almost disappeared (poor contrast on the BF image) while the SAED pattern shows several diffuse diffraction rings that are characteristic of a nearly amorphous material.

Again, a special attention has been devoted to the observation and the identification of the defects created during irradiation. As displayed in Figure 9, around 1.2×10^{14} ions.cm^{-2} (0.3 dpa), TEM images show the appearance of black dots on the BF micrograph, more visible as white dots on the DF image. Although the resolution of the microscope is not sufficient to observe point defects, the observed contrasts indicate the nucleation of strain defect clusters that can be interpreted as nano-loops, nano-voids or nano-accumulation of interstitials. With the increasing fluence, those black dot defects tend to multiply and to grow until the observation of larger stress fields, like dislocation loops at a fluence of 1×10^{15} ions.cm^{-2} (around 2.5 dpa) as it was observed in the previous F_1 thin foil.

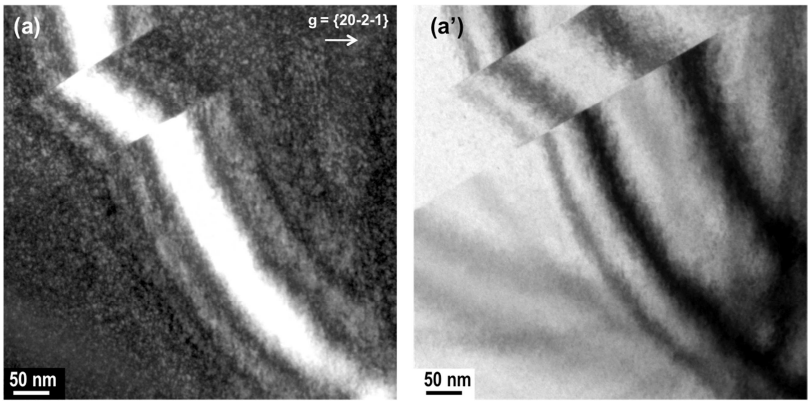

Figure 9 *(1 column)* – *(a): DF image of F_2 thin foil irradiated with 1 MeV Au at RT at a fluence of 1.2×10^{14} ions.cm^{-2} and (a'): corresponding BF image. White and black dots are visible on the DF and BF images respectively (transversal band is a twin imaging).*

Another point is that no evidence of any crystallographic orientation effect was observed during the *in situ* TEM ion irradiation. Indeed, for the F_1 and F_2 thin foils for which the ion beam has been deliberately chosen to be randomly (F_1) or aligned (F_2) along a crystallographic axis of a given grain, the TEM images obtained at different irradiation fluences never show any significant differences between the various grains. With the increasing fluence, the defects created in the grains remain similar whatever the ion beam direction with respect to the grain orientation. This point was especially challenging because during irradiation, due to small distortions, the zone axis slightly changes but the deviation did not exceed the Bragg angle value (i.e. 0.4 degree), which is small enough not to lose the alignment. Therefore, we cannot conclude on a preferential stability under irradiation between the icosahedra and the linear chain that composed the structure of boron carbide.

3.2 Irradiations at 500°C and 800°C

Figure 10 shows the evolution of the F_3 thin foil before and after ion irradiation at 800°C. As it was already observed at the beginning of the RT irradiations, a local curvature of the thin foils related to a material stress occurred, but stabilized more rapidly than at RT (1×10^{13} ions.cm^{-2}). From 1.3×10^{14} ions.cm^{-2} until the end of the irradiation (Figure 10b), the inserted SAED patterns clearly show the appearance of a non-diffuse diffraction ring related to an interplanar distance which does not correspond to any boron carbide crystallographic structure. The same evolution is observed at 500°C (not shown here). Figure 11a shows a SAED pattern of the F_3 thin foil after an irradiation at 500°C at 3×10^{15} ions.cm^{-2} and Figure 11b was taken from a selected part of the diffraction ring (circled zone on the diffraction pattern). The well-defined white dots in the DF image correspond to nanocrystals of another phase. Their size is close of 10 nm. The main modifications observed on the BF images during irradiation correspond principally to the appearance of this new phase. This one is considered as an artifact that prevents the observations of small defects (black dot defects

and even dislocation loops) in the material and makes difficult the comparison of the detailed damage evolution between the thin foils irradiated at 500°C/800°C and at RT.

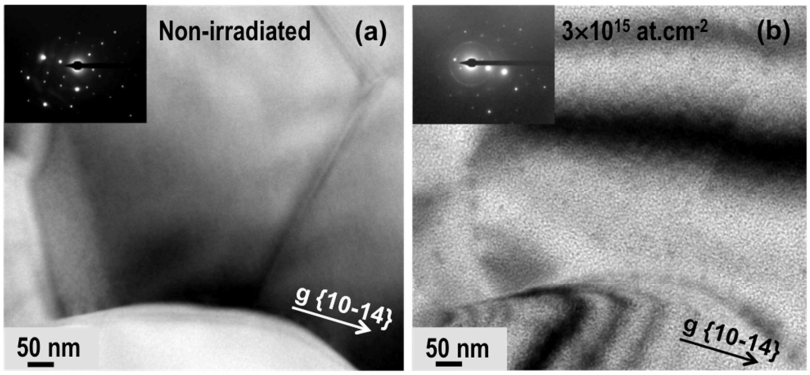

Figure 10 *(1 column)* – *Bright field images showing the evolution of F_3 thin foil irradiated at 800°C at two fluences: (a) non irradiated ; (b) 3×10^{15} ions.cm^{-2}.*

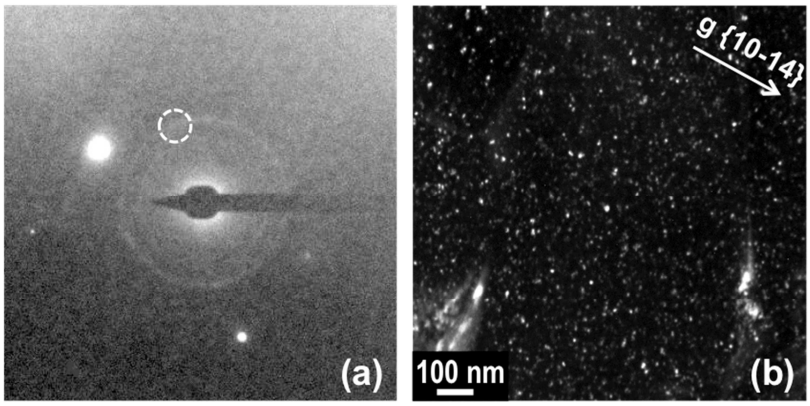

Figure 11 *(1 column)* – *(a) SAED pattern of the F_3 thin foil after irradiation at 500°C at a fluence of 3×10^{15} ions.cm^{-2}. (b) DF image showing the apparition of a new phase, obtained when selecting the ring seen on the SAED pattern at 500°C.*

Comment : the discussion has been divided in several smaller paragraphs, as suggested by the referee, to facilitate easy reading.

4. Discussion

It is interesting to compare the results obtained on the F_1 thin foil containing gold ions with those obtained on the F_2 thin foil which is free of gold ions. Similar defects and amorphization process are observed but with different kinetics. The F_1 thin foil displays a lower amorphization threshold than the F_2 one. This role played by gold ions implanted in boron carbide was already outlined by Gosset *et al.* [30]. They performed TEM examination on boron carbide samples previously irradiated with 4 MeV gold ions. They observed two disctinct amorphization processes depending on the zone of the thin foil without or with gold

atoms. For the latter case, the amorphization process was governed by the concentration of gold atoms inserted in the structure. They observed a full amorphization for a concentration of 0.06 at. % which is much lower than in our experiment (0.15 at. % at the gold profile maximum for a fluence of 10^{15} ions.cm^{-2} - see figure 4). If we consider that amorphization lowers the bulk density, it might be possible that the SRIM calculations would not be accurate and that the concentration profile could be shifted towards the bulk. However, even if we consider a 50 % shift, the concentration would still be higher than 0.06 at. %. To explain this difference, we can assume that the effect of electrons during irradiation prevents or, at least, slows down the amorphization process of boron carbide. This is consistent with previous observations [33] and can be explained by a synergistic effect of electronic stopping power and nuclear stopping power and/or a localized extra heating brought by the electron beam during irradiation that increases the local temperature.

Now we can assume that the results obtained on the F_2 thin foil, which does not contain gold ions and was not irradiated simultaneously by the electron beam and by the gold ions beam, can be used to discuss the damaging and amorphization processes. The successive damaging steps that lead to amorphization can be described as follow.

The first step would be comprised between 0 and 0.5 dpa. In this first step, we have seen the immediate appearance of several bend countours, which progressively disappear until one last countour subsides at around 0.5 dpa. This is linked with the observation of « black dots » apparition at around 0.3 dpa which must be interpreted as the accumulation of point defects which tend to form defects such as nano-loops, nano-voids… This first step clearly corresponds to the creation of point defects by irradiation. There is an accumulation of these defects which begin to nucleate into complex defects. It is still unclear which kinds of point defects are created. However, to the contrary of SiC [45], the nucleation of these small clusters (of a few nanometers in diameter) do not amorphize B_4C.

The second step should be comprised between 0.5 dpa and 7.6 dpa. During this step, we see more and more « black dot defects » together with the appearance of dislocation loops at around 2.5 dpa.

The third and last step corresponds to the amorphization process which begins at 7.6 dpa and is still not total at 10 dpa which corresponds to the maximum irradiation fluence (4×10^{15} ions.cm^{-2}) that we performed. The amorphization threshold found in this work can be compared to other irradiation conditions with charged particles. From literature data of [26], we can calculate, by using the SRIM software, an amorphization threshold of 1.5 dpa for the H^+ ion-irradiation (fluence of 2.5×10^{17} ions.cm^{-2}). From their double irradiation (H_2^+ ions with He^+ ions), we can calculate an amorphization threshold of 1.7 dpa (0.3 dpa due to H ions and 1.4 dpa due to He ions). Those values are lower than the one calculated by Gosset *et al.* (2 dpa) which is well below our value of 7.6 dpa. All these irradiations were made at RT, so

the temperature cannot explain these discrepancies. The « low » amorphization thresholds of 1.5 dpa and 1.7 dpa are certainly due to the high concentration of ions in the structure or by the high flux used in this experiment (2×10^{14} ions.cm^{-2}.s^{-1}). The difference between the amorphization threshold of our work and those of Gosset *et al.* are more difficult to explain because the irradiation conditions are very close. The only significant difference is that Gosset *et al.* observed by TEM a thin foil containing gold atoms. The observed zone, free of gold atoms, is near the surface which can impact the creation rate of defects enhancing the amorphization process. Moreover, it has already been shown that amorphization can be stimulated near a crystalline/amorphous interface [46]. The last hypothesis is that the grain size distribution is really different and that grain boundaries play a role in the amorphization process. If we refer to the work of Weber who has reviewed the different irradiation-induced amorphization processes in [47], we can identify a heteregenous mechanism, which is probably driven by local accumulation of high defect concentrations due to the overlap of collision cascades. B_4C is clearly very resistant to ballistic irradiation as the amorphization still does not occur at 10 dpa. This should also indicate that there is a competitive effect between the damage accumulation and the self-healing of the structure even at RT. It could be possible that as the electronic stopping power is not negliglible (4.7 keV.nm^{-1}) in our irradiation conditions, it can slow down the kinetic rate of amorphization. However Gosset *et al.* have almost the same value and they observed a lower value of amorphization threshold which shows that the electronic stopping power impact should not be significant.

At least, we have performed some irradiations at different temperatures. It is well known that the increase of temperature allows defect annealing and so prevent, or at least delays, the amorphization process [34]. In our experiment, at both temperatures, 500 °C and 800 °C, no amorphization of the material occurred until a damage rate of 7.5 dpa, despite a concentration of implanted Au atoms in the thin foils, the TEM lamella thickness being larger than 180 nm (see Table 1). The irradiation at 500 °C and 800 °C led to the formation of a new phase, not observed at RT. This phase grew with the increasing fluence preventing a complete analysis of the defect formation. A measure of the two diffraction ring diameters in both thin foils gave us the following values: the more intense diffraction ring corresponds to an interplanar distance of 2.1 Å. The other ring corresponds to a distance of 2.7 Å. The examination of the powder diffraction file (JCPDS) shows the better agreement for the AuB_2 compound with two intense diffraction lines at 2.15 Å and 2.72 Å. Concerning the hex-B_2O_3 compound, two diffraction lines could match (respectively 2.09 Å and 2.79 Å) but an intermediate line should also be visible at 2.24 Å. Furthermore, as described before, the thicknesses of F_3 and F_4 thin foils are larger than the projected range of the Au^+ ions (see Table 1) so that the presence of Au atoms is expected and the assumption of the formation of an AuB_2 phase is the most probable.

5. Conclusions

The ballistic damage created in boron carbide pellets irradiated with 1 MeV Au^+ ions were studied *in situ* by TEM at three different temperatures (RT, 500°C, 800°C).

First, no particular effect of the crystallographic orientation of the grains with respect to the ion beam was highlighted in this experiment.

Differences are seen between the two thin foils irradiated at RT. We observed that the presence of Au atoms inside the matrix accelerates the amorphization process but that the damage is similar in both cases. For the thin foil free of gold atoms, several steps of damage formation, leading to an heteregeneous amorphization are observed:

- Step 1 (0 to 0.5 dpa): Production of point defects by irradiation which nucleate into strained nano-clusters (typical size of a few nanometers).
- Step 2 (0.5 to 7.6 dpa): Multiplication and growing of these small clusters. Dislocation loops (typical size of 20 nm) are observed at 2.5 dpa.
- Step 3 (from 7.6 dpa): Amorphization starts. The amorphization process is not total at 10 dpa corresponding to our maximum irradiation fluence of 4×10^{15} ions.cm^{-2}.

At 500°C and 800°C, the appearance of an extra artifact phase on the thin foils prevented the defect formation. However, we can still assume that no amorphization of the material occurred for a damage rate of 7.5 dpa. The temperature allows a self-healing of the defects and prevents the amorphization process.

~~In the near future, other experiments that are being performed using Raman spectroscopy could give us more information on the behavior of the structural elements, central chain and icosahedron, in ion irradiated boron carbide~~.

Acknowledgements

This work was financially supported by the NEEDS Program of the CNRS. The authors would like to thank all the JANNuS-Orsay technical staff for their precious assistance during the irradiation sessions. Thanks are also due to the CLYM (Centre LYonnais de Microscopie: www.clym.fr) for the access to the FIB/SEM Zeiss NVISION 40 and to the TEM JEOL 2010F.

References

[1] F. Thévenot, *Boron carbide - A comprehensive review*, J. Eur. Ceram. Soc. 6 (1990) 205-225.

[2] T. Inoue, T. Onchi, H. Kôyama, H. Suzuki, *Irradiation effects of boron carbide used as control rod elements in fast breeder reactors*, J. Nucl. Mater. 74 (1978) 114-122.

[3] H. Suzuki, T. Maruyama, T. Wakasa, *Postirradiation Annealing of Boron Carbide Pellet Irradiated in Fast Breeder Reactor*, J. of Nucl. Sci. Technol. 16 (1979) 588-595.

[4] G. Locatelli, M. Mancini, N. Todeschini, *Generation IV nuclear reactors: Current status and future prospects*, Energ. Policy 61 (2013) 1503-1520.

[5] K. Aoto, P. Dufour, Y. Hongyi, J.P. Glatz, Y.-i. Kim, Y. Ashurko, R. Hill, N. Uto, *A summary of sodium-cooled fast reactor development*, Prog. Nucl. Energ. 77 (2014) 247-265.

[6] M.S. Chenaud, N. Devictor, G. Mignot, F. Varaine, C. Venard, L. Martin, M. Phelip, D. Lorenzo, F. Serre, F. Bertrand, N. Alpy, M. Le Flem, P. Gavoille, R. Lavastre, P. Richard, D. Verrier, D. Schmitt, *Status of the Astrid Core at the End of the Pre-Conceptual Design Phase 1*, Nucl. Eng. Technol. 45 (2013) 721-730.

[7] D. Gosset, B. Provot, *Boron carbide as a potential inert matrix: an evaluation*, Prog. Nucl. Energ. 38 (2001) 263-266.

[8] D. Simeone, C. Mallet, P. Dubuisson, G. Baldinozzi, C. Gervais, J. Maquet, *Study of boron carbide evolution under neutron irradiation by Raman spectroscopy*, J. Nucl. Mater. 277 (2000) 1-10.

[9] V. Domnich, S. Reynaud, R.A. Haber, M. Chhowalla, *Boron Carbide: Structure, Properties, and Stability under Stress*, J. Am. Ceram. Soc. 94 (2011) 3605-3628.

[10] A. Jay, N. Vast, J. Sjakste, O. Hardouin Duparc, *Carbon-rich icosahedral boron carbide designed from first principles*, Appl. Phys. Lett. 105 (2014) 031914.

[11] P.F. Rogl, J. Vřešťál, T. Tanaka, S. Takenouchi, *The B-rich side of the B–C phase diagram*, Calphad 44 (2014) 3-9.

[12] M. Bouchacourt, F. Thevenot, *The properties and structure of the boron carbide phase*, J. Less Common Metals 82 (1981) 227-235.

[13] S. Aryal, P. Rulis, WY Ching, *Mechanism for amorphization of boron carbide B_4C under uniaxial compression*, Phys. Rev. B, 84 (2011) 184112.

[14] X.Q. Yan, Z. Tang, L. Zhang, Y. Zhang, T. Goto, J.W. McCauley, M.W. Chen, *Depressurization Amorphization of Single-Crystal Boron Carbide*, Phys. Rev. Lett. 102 (2009) 075505.

[15] G. Fanchini, J.W. McCauley, M. Chhowalla, *Behavior of disordered boron carbide under stress*, Phys. Rev. Lett. 97 (2006) 035502.

[16] X.Q. Yan, W.J. Li, T. Goto, M.W. Chen, *Raman spectroscopy of pressure-induced amorphous boron carbide*, Appl. Phys. Lett. 88 (2006) 131905.

[17] M. Chen, J.W. McCauley, KJ. Hemker, *Shock-Induced Localized Amorphization in Boron Carbide*, Science 299 (2003) 1563-1566.

[18] S. Zhao, B. Kad, B. A. Remington, J. C. LaSalviac, C. E. Wehrenberg, K. D. Behler and M. A. Meyers, *Directional amorphization of boron carbide subjected to laser shock compression*, PNAS 113 (2016) 12088-12093.

[19] D. Ge, V. Domnich, T. Juliano, E. Stach, Y. Gogotsi, *Structural damage in boron carbide under contact loading*, Acta Mater. 52 (2004) 3921-3927.

[20] G. Subhash, D. Ghosh, J. Blaber, J.Q. Zheng, V. Halls, K. Masters, *Characterization of the 3-D amorphized zone beneath a Vickers indentation in boron carbide using Raman spectroscopy*, Acta Mater. 61 (2013) 3888-3896.

[21] D. Ghosh, G. Subhash, T.S. Sudarshan, R. Radhakrishnan, X.-L. Gao, *Dynamic Indentation Response of Fine-Grained Boron Carbide*, J. Am. Ceram. Soc. 90 (2007) 1850-1857.

[22] M.K. Reddy, P. Liu, A. Hirata, T. Fujita, M.W. Chen, *Atomic structure of amorphous shear bands in boron carbide*, Nat. Commun. 4 (2013) 2483.

[23] K.Y. Xie, Q. An, T. Sato, A.J. Breen, S.P. Ringer, W.A. Goddard III, J.M. Cairney and K.J. Hemker, Breaking the icosahedra in boron carbide, PNAS 113 (2016) 12012–12016.

[24] D. Simeone, D. Gosset, D. Quirion, X. Deschanels, *Study of B_4C microstructure evolution under neutron irradiation by X-ray diffraction profiles analysis*, J. Nucl. Mater. 264 (1999) 295-308.

[25] A. Jostsons, C.K.H. Dubose, *Microstructure of boron carbide after fast neutron irradiation*, J. Nucl. Mater. 44 (1972) 91-95.

[26] K.N. Kushita, K. Hojou, S. Furuno, *In-situ EELS and TEM observation of boron-carbide (B_4C) during hydrogen-ion and helium-ion bombadments*, Microsc. Microanal. M. 6 (1995) 149-157.

[27] T. Maruyama, M. Iwanami, S. Ohnuki, T. Suda, S. Watanabe, K. Ikezawa, *Precipitation and amorphization in boron carbide irradiated by high energy helium ions*, Effects of Radiation on Materials: 21st International Symposium; Book Series: AMERICAN SOCIETY FOR TESTING AND MATERIALS SPECIAL TECHNICAL PUBLICATION ; Volume: 1447 ; Pages: 670-679 ; DOI: 10.1520/STP11265S ; Published: 2004).

[28] G. Victor, Y. Pipon, N. Bérerd, N. Toulhoat, N. Moncoffre, N. Djourelov, S. Miro, J. Baillet, N. Pradeilles, O. Rapaud, A. Maître, D. Gosset, *Structural modifications induced by ion irradiation and temperature in boron carbide B_4C*, Nucl. Instrum. Meth. B 365 (2015) 30-34.

[29] D. Gosset, S. Miro, S. Doriot, G. Victor, V. Motte, *Evidence of amorphisation of B_4C boron carbide under slow, heavy ion irradiation*, Nucl. Instrum. Meth. B 365 (2015) 300-304.

[30] D. Gosset, S. Miro, S. Doriot, N. Moncoffre, *Amorphisation of boron carbide under slow heavy ion irradiation*, J. Nucl. Mater. 476 (2016) 198-204.

[31] H.M. H. Inui, H. Fujita, *Electron irradiation induced crystalline-amorphous transition in ceramics*, Acta Metall. 37 (1988) 1337-1342.

[32] H. Mori, T. Sakata, H. Inui, *High-resolution electron-microscope studies of irradiation-induced crystalline-to-amorphous transistion in boron carbide*, Phil. Mag. Lett. 61 (1990) 49-53.

[33] M. Carrard, D. Emin, L. Zuppiroli, *Defect clustering and self-healing of electron-irradiated boron-rich solids*, Phys. Rev. B 51 (1995) 11270-11274.

[34] Y. Serruys, P. Trocellier, S. Miro, E. Bordas, M.O. Ruault, O. Kaïtasov, S. Henry, O. Leseigneur, T. Bonnaillie, S. Pellegrino, S. Vaubaillon, D. Uriot, *JANNUS: A multi-irradiation platform for experimental validation at the scale of the atomistic modelling*, J. Nucl. Mater. 386-388 (2009) 967-970; A. Gentils, C. Cabet, *Investigating radiation damage in nuclear*

energy materials using JANNuS multiple ion beams, submitted to Nucl. Instrum. Methods B (2018).

[35] S. Hayun, S. Kalabukhov, V. Ezersky, M.P. Dariel, N. Frage, *Microstructural characterization of spark plasma sintered boron carbide ceramics*, Ceram. Int. 36 (2010) 451-457.

[36] X. Li, D. Jiang, J. Zhang, Q. Lin, Z. Chen, Z. Huang, *Densification behavior and related phenomena of spark plasma sintered boron carbide*, Ceram. Int. 40 (2014) 4359-4366.

[37] N. Mortazavi, M. Esmaily, M. Halvarsson, *The capability of Transmission Kikuchi Diffraction technique for characterizing nano-grained oxide scales formed on a FeCrAl stainless steel*, Mater. Lett. 147 (2015) 42-45.

[38] G.C. Sneddon, P.W. Trimby, J.M. Cairney, *Transmission Kikuchi diffraction in a scanning electron microscope: A review*, Mater. Sci. Eng R 110 (2016) 1-12.

[39] T. Malis, S.C. Cheng, R.F. Egerton, *EELS log ratio technique for specimen-thickness measurement in the TEM,* J. Electron Micr. Tech. 8 (1988) 193.

[40] C.-O. Bacri, C. Bachelet, C. Baumier, J. Bourçois, L. Delbecq, D. Ledu, N. Pauwels, S. Picard, S. Renouf, C. Tanguy, *SCALP, a platform dedicated to material modifications and characterization under ion beam*, Nucl. Instrum. Meth. B 406 (2017) 48-52.

[41] J.F. Ziegler, M.D. Ziegler, J.P. Biersack, *SRIM – The stopping and range of ions in matter (2010)*, Nucl. Instrum. Meth. B 268 (2010) 1818-1823.

[42] CEA, e-den, "Les réacteurs nucléaires à caloporteur sodium", 2014.

[43] J. Frantz, J. Tarus, K. Nordlund, J. Keinonen, *Mechanism of electron-irradiation-induced recrystallization in Si*, Phys. Rev. B 64 (2001) 125313.

[44] I. Jencic, M.W. Bench, I.M. Robertson, M.A. Kirk, *Electron-beam-induced crystallization of isolated amorphous regions in Si, Ge, GaP, and GaAs*, J. Appl. Phys. 78 (1995) 974-982.

[45] F. Gao, W.J. Weber, R. Devanathan, *Defect production, multiple ion–solid interactions and amorphization in SiC*, Nucl. Instrum. Meth. B 191 (2002) 487-496.

[46] H.A. Atwater, J.S. Im, W.L. Brown, *Heterogeneous amorphization of Si during ion irradiation: dependence of amorphous Si nucleation kinetics on defect energy and structure*, Nucl. Instrum. Meth. B 59-60 (1991) 386-390.

[47] W.J. Weber, *Models and mechanisms of irradiation-induced amorphization in ceramics*, Nucl. Instrum. Meth. B 166-167 (2000) 98-106.